Clim Dyn (2014) 43:1715–1730
DOI 10.1007/s00382-013-2000-9

Indian Ocean variability in the CMIP5 multi-model ensemble: the zonal dipole mode

Lin Liu · Shang-Ping Xie · Xiao-Tong Zheng · Tim Li · Yan Du · Gang Huang · Wei-Dong Yu

Received: 9 July 2013 / Accepted: 8 November 2013 / Published online: 22 November 2013

Abstract The performance of 21 Coupled Model Intercomparison Project Phase 5 (CMIP5) models in the simulation of the Indian Ocean Dipole (IOD) mode is evaluated. Compared to CMIP3, CMIP5 models exhibit a similar spread in IOD intensity. A detailed diagnosis was carried out to understand whether CMIP5 models have shown improvement in their representation of the important dynamical and thermodynamical feedbacks in the tropical Indian Ocean. These include the Bjerknes dynamic air-sea feedback, which includes the equatorial zonal wind response to sea surface temperature (SST) anomaly, the thermocline response to equatorial zonal wind forcing, the ocean subsurface temperature response to the thermocline variations, and the thermodynamic air-sea coupling that includes the wind-evaporation-SST and cloud-radiation-SST feedback. Compared to CMIP3, the CMIP5 ensemble produces a more realistic positive wind-evaporation-SST feedback during the IOD developing phase, while the simulation of Bjerknes dynamic feedback is more unrealistic especially with regard to the wind response to SST forcing and the thermocline response to surface wind forcing. The overall CMIP5 performance in the IOD simulation does not show remarkable improvements compared to CMIP3. It is further noted that the El Niño-Southern Oscillation (ENSO) and IOD amplitudes are closely related, if a model generates a strong ENSO, it is likely that this model also simulates a strong IOD.

Keywords Indian Ocean Dipole zonal model · CMIP3 · CMIP5 · Interannual variability · Bjerknes feedback · Thermodynamic feedback

1 Introduction

As the significant interannual variability in tropical Indian Ocean region, the Indian Ocean Dipole (IOD) is known as a basin-scale ocean–atmosphere coupled mode (Saji et al.

L. Liu (✉) · W.-D. Yu
Center for Ocean and Climate Research, First Institute of Oceanography, State Oceanic Administration (SOA), Qingdao 266061, China
e-mail: liul@fio.org.cn

S.-P. Xie
Scripps Institution of Oceanography, University of California, San Diego, La Jolla, CA, USA

S.-P. Xie · X.-T. Zheng
Physical Oceanography Laboratory, Ocean University of China, Qingdao, China

T. Li
International Pacific Research Center and Department of Meteorology, University of Hawaii at Manoa, Honolulu, HI, USA

Y. Du
State Key Laboratory of Tropical Oceanography, South China Sea Institute of Oceanology, Chinese Academy of Sciences, Guangzhou, China

G. Huang
Key Laboratory of Regional Climate-Environment Research for Temperate East Asia, Institute of Atmospheric Physics, Chinese Academy of Sciences, Beijing, China

G. Huang
Collaborative Innovation Center on Forecast and Evaluation of Meteorological Disasters, Nanjing University of Information Science and Technology, Nanjing, China

1999; Webster et al. 1999) with great impacts on climate variability in Africa, South Asia, East Asia, and other remote regions (e.g., Saji and Yamagata 2003a, b; Ashok et al. 2004; Yu et al. 2005; Behera et al. 2005; England et al. 2006; Wang et al. 2006; Liu et al. 2013; Du et al. 2013a). The seesaw distributions of anomalous positive/negative sea surface temperature (SST) in the southeastern IO (SEIO) off Java-Sumatra and negative/positive in the western IO (WIO), accompanied by pronounced anomalous westerlies/easterlies over the central equatorial IO (CEIO) compose the spatial pattern of classic IOD events. One of the notable features of IOD is the phase locking phenomena as IOD events always rapidly developing in boreal summer and reaching the mature phase in boreal fall. Previous studies illustrate that both positive and negative dynamical, and thermodynamic feedback mechanisms (Bjerknes 1966, 1969; Xie and Philander 1994; Webster et al. 1999; Li et al. 2003) are responsible for the evolution of IOD events, which include the Bjerknes feedback and thermodynamic feedback. The Bjerknes feedback indicates a decrease in zonal SST gradient, caused for instance by a relaxation of the tilt of the thermocline, implies a reduction of the zonal wind stress that will amplify the initial perturbation. The thermodynamic feedback includes wind-evaporation-SST feedback and cloud-radiation-SST feedback (Li et al. 2003, 2011; Cai and Qiu 2013; Weller and Cai 2013). As the useful tools for the prediction, current state-of-art climate models have the ability to simulate and predict the IOD evolution and amplitude as well as the relevant remote impact (Luo et al. 2007, 2008). A large number of studies have been performed to assess and evaluate the performance of simulated IOD events in coupled general circulation models (CGCM) (e.g., Yamagata et al. 2004; Cai et al. 2005, 2011; Zhong et al. 2005; Saji et al. 2006; Luo et al. 2007; Song et al. 2007; Zheng et al. 2010; Cai and Cowan 2013). Liu et al. 2011 further evaluated the simulated IOD events performance in 23 CMIP3 models with the aim to assess the different internal feedback mechanisms. The research introduced a combined Bjerknes and thermodynamic feedback intensity index, which gives a quantitative measure of the relative contribution of the dynamic and thermodynamic feedback processes during IOD evolutions.

In order to provide the up-to-date climate change experiments for assessment in the Intergovernmental Panel on Climate Change (IPCC) Fifth Assessment Report, the fifth phase of the Coupled Model Intercomparison Project (CMIP5) was organized by World Climate Research Programme (WCRP) Working Group Coupled Models Climate Simulation Panel. CMIP5 represents the largest and most comprehensive international global coupled climate model experiment and multi-model analysis effort ever attempted (Meehl et al. 2009; Taylor et al. 2012). It collected CGCM experiments targeted to twentieth- and twenty-first-century climate simulations as well as climate change experiments. Since the models participating CMIP5 program represents state of the art, the performance in simulated IOD events should be carefully evaluated to answer whether IOD features and associated feedback mechanism simulated in CMIP5 is better or not than in CMIP3.

The objective of the present study is to conduct a detailed diagnosis of the dynamic and thermodynamic feedbacks associated with IOD from 21 CGCMs that participated in CMIP5 with the comparison to the performance in CMIP3. The rest of the paper is organized as follows. Section 2 briefly describes the datasets used. Section 3 examines the IOD simulations from the 21 CGCMs. Section 4 investigates the dynamic and thermodynamic coupling strength. The relationship of the air-sea coupling strength to the background mean state is examined in Sect. 5. Section 6 discusses the possible cause of misrepresentation of the cloud-radiation-SST feedback in some CMIP5 models and the relationship between IOD and ENSO events. Finally, a summary is given in Sect. 7.

2 Data

The primary datasets used for this study are the outputs of available 21 models from the CMIP5 datasets. The model variables used in the diagnosis include three-dimensional ocean temperature, current, surface wind, cloud fraction, and surface heat flux fields. Table 1 lists information for all 21 models used in this study. Further detailed information can be obtained at the following website (http://cmip-pcmdi.llnl.gov/cmip5).

The particular datasets analyzed here are so-called Climate of the Twentieth-Century Experiment (historical run). The forcing agents of this experiment include greenhouse gases (CO_2, CH_4, N_2O, and Chlorofluorocarbons), aerosol direct effects, volcanoes, and solar forcing (Taylor et al. 2012). The results reported in this analysis were only for the period between January 1950 and December 1999 in order to compare with observational datasets. The climatological annual cycle was defined based on this 50-year period. The interannual anomalies were then obtained by subtracting the monthly mean variables from their respective climatological annual cycles.

For comparison of the model simulations with observations, various observed and reanalyzed (assimilated) atmospheric and oceanic datasets were used. Three-dimensional atmospheric wind fields, surface latent heat flux, cloud cover, and net surface short wave radiation were obtained from the National Centers for Environmental Prediction and the National Center for Atmospheric

Table 1 List of 21 CMIP5 models and the observation

No.	DMI	CMIP model names
1	0.37	GISS-E2-H
2	0.39	GISS-E2-R
3	0.45	MRI-CGCM3
4	0.49	IPSL-CM5A-LR
5	0.59	IPSL-CM5A-MR
6	0.61	FIO-ESM
7	0.62	BCC-CSM1.1
8	0.66	HadCM3
9	0.69	CanESM2
10	0.70	NorESM1-ME
11	0.72	ACCESS1.0
12	0.76	MIROC5
13	0.77	HadGEM2-ES
14	0.79	HadGEM2-AO
15	0.80	HadGEM2-CC
16	0.81	NorESM1-M
17	0.89	CNRM-CM5
18	0.95	MPI-ESM-LR
19	1.07	FGOALS-s2
20	1.17	BNU-ESM
21	1.18	CSIRO-Mk3.6.0
22	0.42	Obs

The second column shows the DMI strength value for each model. The third column presents the official name of each model. DMI strength is calculated based on the period from 1950 to 1999. The models have been sorted by DMI strength

Research (NCEP/NCAR) reanalysis (Kistler et al. 2001) and ECMWF 40-year Re-analysis (ERA40) (Simmons and Gibson 2000), and three-dimensional ocean temperatures were obtained from the Simple Ocean Data Assimilation (SODA 2.0.4) reanalysis (Carton et al. 2000) and JMA subsurface temperature by Ishii Ocean Analyses Project (Ishii and Kimoto 2009). In addition, we used the Hadley Centre Global Sea Ice and Sea Surface Temperature (HadISST) product (Rayner et al. 2003) and Extended Reconstruction of Global Sea Surface Temperatures (ERSST) (Smith and Reynolds 2003). Except for the ERA40, which was available from January 1958 to December 1999, the others, others were available for the 50-year period (from January 1950 to December 1999).

3 IOD simulations from CMIP5 models

Figure 1 shows the standard deviation (STD) of sea surface temperature anomaly (SSTA), averaged over 90E–110E, 0–10S, from observations and 21 CMIP5 models. Some models generate a strong IOD variability, whereas others show a relatively weak one. All the models are able to reproduce the maximum SSTA variability in the SEIO off Java-Sumatra but the variance is too large in CMIP5 models than in observations. In general, the multi-model averaged interannual variations in SST are stronger than in observations, similar to CMIP3 models (Cai et al. 2011; Liu et al. 2011). Despite the difference in IOD intensity, CMIP5 models all exhibit a common seasonality that the maximum STD of the zonal SSTA gradient appears in boreal fall season (Fig. 2). Thus the phase locking of IOD is well reproduced. The result is consistent with Saji et al. (2006) and Liu et al. (2011), based on CMIP3 models. Figure 2 compares the dipole mode index (DMI) between observations and the CMIP3 and CMIP5 ensemble means. The DMI for CMIP5 is slightly more realistic than for CMIP3, especially in the IOD developing phase (boreal July, August, and September (JAS) season). The ensemble averaged IOD amplitude from CMIP5 is close to observations during May, June, and July with a smaller intermodal spread than for different CMIP3. In the subsequent 3 months, the ensemble averaged IOD strength from CMIP5 is reduced by around 40 % compared with CMIP3.

We use the DMI defined by Saji et al. (1999), which measures the zonal SST gradient between western and eastern tropical Indian Ocean. We also calculated other indices defined such as the Sumatra cooling index (Xie et al. 2002; Du et al. 2005, 2008; Luo et al. 2010) and a combined SST-wind index (Liu et al. 2011), and the result is quite similar.

Based on the DMI values, the 21 models are classified into three groups, a strong IOD group [withσ(DMI) > 0.8], a moderate IOD group [$0.63 < \sigma(\text{DMI}) < 0.8$] and a weak IOD group [$\sigma(\text{DMI}) < 0.63$]. The strong IOD group includes 7 models, namely HadGEM2-CC, NorESM1-M, CNRM-CM5, MPI-ESM-LR, FGOALS-s2, BNU-ESM and CSIRO-Mk3.6.0. The weak IOD group consists of 7 models, GISS-E2-H, GISS-E2-R, MRI-CGCM3, IPSL-CM5A-LR, IPSL-CM5A-MR, FIO-ESM and BCC-CSM1.1. The result is similar with the previous research (Cai and Cowan 2013).

A composite analysis is conducted to reveal the robust differences between the strong and weak groups. Figure 3 shows the composite anomalies for surface zonal wind, SST, and 20 °C isothermal depth in boreal fall (Sept–Oct–Nov, SON) during positive IOD events (with negative SSTA in the SEIO). Note that the amplitude of the zonal wind in the strong composite is 1.8 m s^{-1}, much larger than that (0.8 m s^{-1}) in the weak composite. The composite SSTA variability in the SEIO also shows a contrast (0.4 vs 0.2 K) between the strong and weak groups. The thermocline depth, represented by 20 °C isothermal depth anomaly, also shows a marked difference in the strong and weak composites. The maximum of the thermocline shoaling is 24 m in the strong

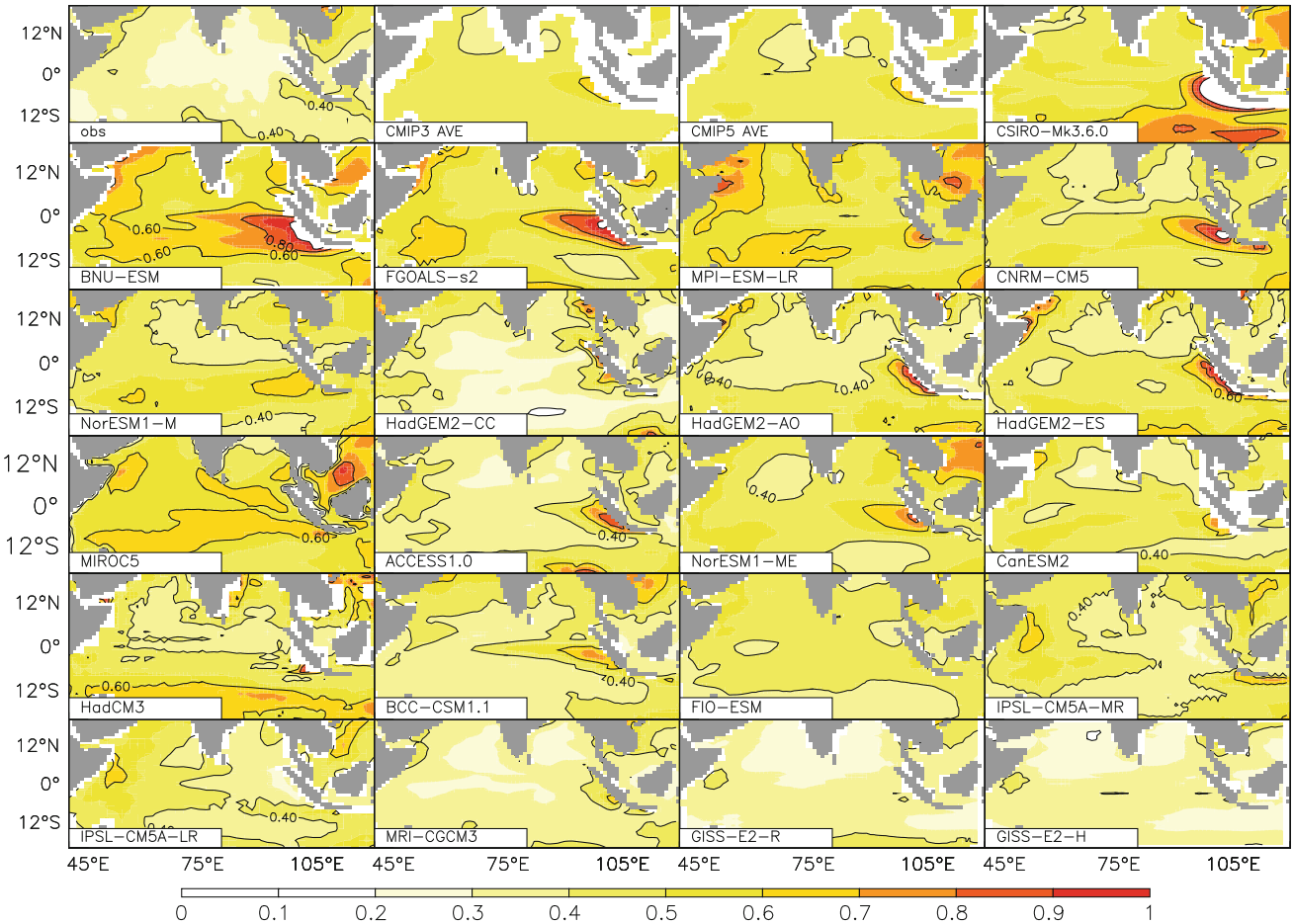

Fig. 1 Standard deviation of SSTA (*shading*, unit: K) fields in SON from the observation (*Obs*), CMIP3 and CMIP5 model ensemble mean (CMIP3 AVE, CMIP5 AVE) and each CMIP5 models

composite, which is 4 times greater than that in the weak composite. In the equatorial region, the maximum thermocline depth variability is primarily confined in the SEIO in both groups.

The temporal evolution of the composite SSTA in the SEIO (figure not shown) shows a peak phase in boreal fall in both the strong and weak composites. A similar evolution feature is found in the zonal wind anomaly field.

4 Measuring dynamic and thermodynamic air-sea coupling

The composite results above illustrate a remarkable difference in the zonal wind, SST and thermocline depth anomalies between the strong and weak groups. Therefore, a hypothesis is suggested that these differences may explain why various models simulate the IOD strength differently. Our previous research had pointed out that the dynamic and thermodynamic coupling strength in each model during the developing phase in JAS was responsible for the diversity in simulated IOD strength in CMIP3 models (Liu et al. 2011). Furthermore, we need to answer the question of which air-sea coupling processes contribute to these differences in the CMIP5 models. In this section, we calculate the dynamic and thermodynamic coupling coefficients among the CMIP5 models.

4.1 Bjerknes feedback

We examine the Bjerknes feedback strength in all models. This dynamic air-sea feedback consists of three processes. The first is how the atmospheric low-level wind responds to the SSTA forcing in the SEIO. It is well known that during the IOD development period (JAS), the most significant feature of SSTA is the dipole pattern. Such a zonal SSTA gradient causes a zonal wind response in the CEIO through the SST-gradient-induced pressure gradient in the atmospheric planetary boundary layer (Lindzen and Nigam 1987) or the mid-tropospheric heating anomaly (Gill 1980).

Figure 4 shows the relationship between the SSTA in the SEIO (90–110°E, 10°S-0) and the zonal wind

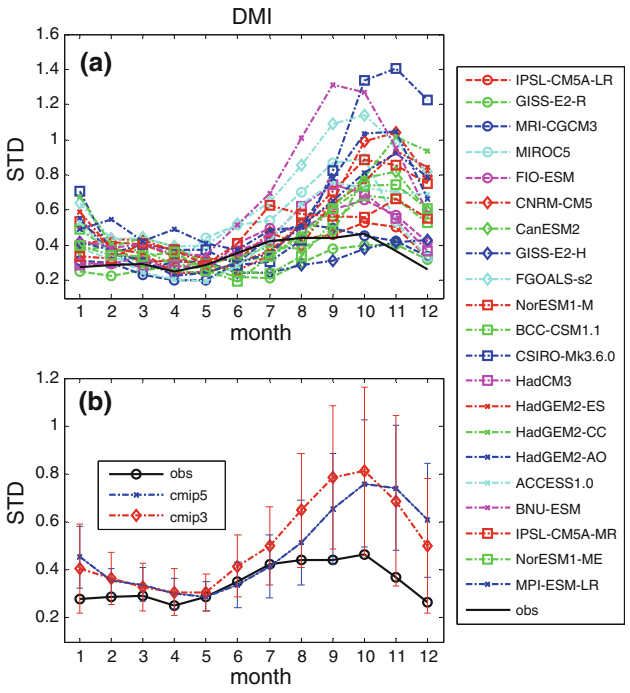

Fig. 2 Monthly standard deviations of DMI from 21 CMIP5 coupled models and the observation (**a**, unit: K) and the monthly standard deviations of DMI from ensemble mean of 21 CMIP5 models (*cmip5*), 23 CMIP3 models (*cmip3*) and the observation (*obs*) (**b**, unit: K). The *error bar* indicates the standard deviation spread among coupled models. The detailed information on CMIP3 models referred to Liu et al. (2011)

anomalies in the CEIO (70–90°E, 5°S–5°N) from the 21 models. For comparison, the observed SST-wind relationship is plotted in each subplot. Consistent with the observed relationship, all of the models exhibit a positive correlation between the zonal wind and SST anomalies, that is, a negative SSTA in the SEIO (which corresponds to a positive IOD event according to Saji et al. (1999)) is accompanied with an easterly anomalies in the CEIO.

We hereby denote a SST-wind coupling coefficient, R(u, T), to represent how strong the low-level wind responds to a unit SSTA forcing at each model. Mathematically, it equals to the linear slope in each of scatter diagrams in Fig. 4, calculated based on the least square fitting method. It is interesting to note that the averaged slope in the strong composite is about 1.7 m s^{-1} K^{-1}, much larger than the averaged slope (1.0 m s^{-1} K^{-1}) in the weak composite. Compared to the observed R(u, T), the SST-wind coupling coefficient in the strong group appears more realistic.

The second process of Bjerknes feedback involves how the ocean thermocline responses to the equatorial surface wind forcing. Figure 5 shows the scatter diagrams between anomalies of zonal wind in the CEIO and the thermocline depth in the SEIO for each model. The observed feedback relationship between the wind and SEIO thermocline depth is positive because an easterly wind anomaly in the CEIO may lift (suppress) the thermocline in the eastern (western) part of the basin. Such a positive relationship is captured by all of the coupled models.

We denote a wind-thermocline coupling coefficient R(D, u) to measure the strength of thermocline depth change for a given unit zonal wind forcing. It can be represented by the slope in Fig. 5. The averaged R(D, u) for the strong composite is 4.9 m per m s^{-1}, while it is about 6.3 m per m s^{-1} for the weak composite. The observed R(D, u) is weaker than either of Bjerknes feedback values.

The third process involves how the ocean subsurface temperature responds to the ocean thermocline variation. In the SEIO, a shoaling (deepening) of the thermocline leads to a negative (positive) temperature anomaly at a fixed subsurface level. The change of the subsurface temperature may further affect SST through the anomalous vertical temperature advection by the mean upwelling. In the region of deep climatological mean thermocline, the subsurface temperature effect is small on SST variability.

Figure 6 shows the observed and the simulated relationship between anomalies of the thermocline depth and the temperature at 70 m in the SEIO. A positive correlation appears between the observed thermocline depth and subsurface temperature. We hereby denote R(Te, D) as a thermocline-subsurface temperature coupling coefficient, which can be measured by the slope in Fig. 6. The observed slope is 0.1 K m^{-1}, implying that one meter thermocline change would lead to a subsurface temperature change of 0.1 K. All of the CMIP5 models reproduce such a positive relationship, even though the slope is markedly different. The comparison of the strong versus the weak composite shows that the thermocline-subsurface temperature feedback in the former is about 10 % greater than that in the latter.

The overall Bjerknes dynamic feedback strength could be determined by the combined effect of the three processes above. To quantitatively measure the Bjerknes feedback intensity and to compare it with the thermodynamic feedback intensity, we induce it from the simplified SST tendency equation with $T' = \delta T e^{\sigma t}$ as below:

$$\rho C_w h \sigma = \rho C_w \bar{w} \frac{T'_e}{T'} + \frac{Q'}{T'} \quad (1)$$

where T' and T'_e denote the surface and subsurface ocean temperature anomalies respectively (more detailed refer to Liu et al. 2011), $\bar{w}$ denotes the climatological mean vertical velocity at the base of the ocean mixed layer, Q' is the net surface heat flux anomaly, ρ and C_w are the sea water density and specific heat, and h is the ocean mixed layer depth. Here the left hand side of Eq. (1) is proportional to the growth rate (σ) of the SSTA. The second term in the right hand side of Eq. (1) represents how strong the surface

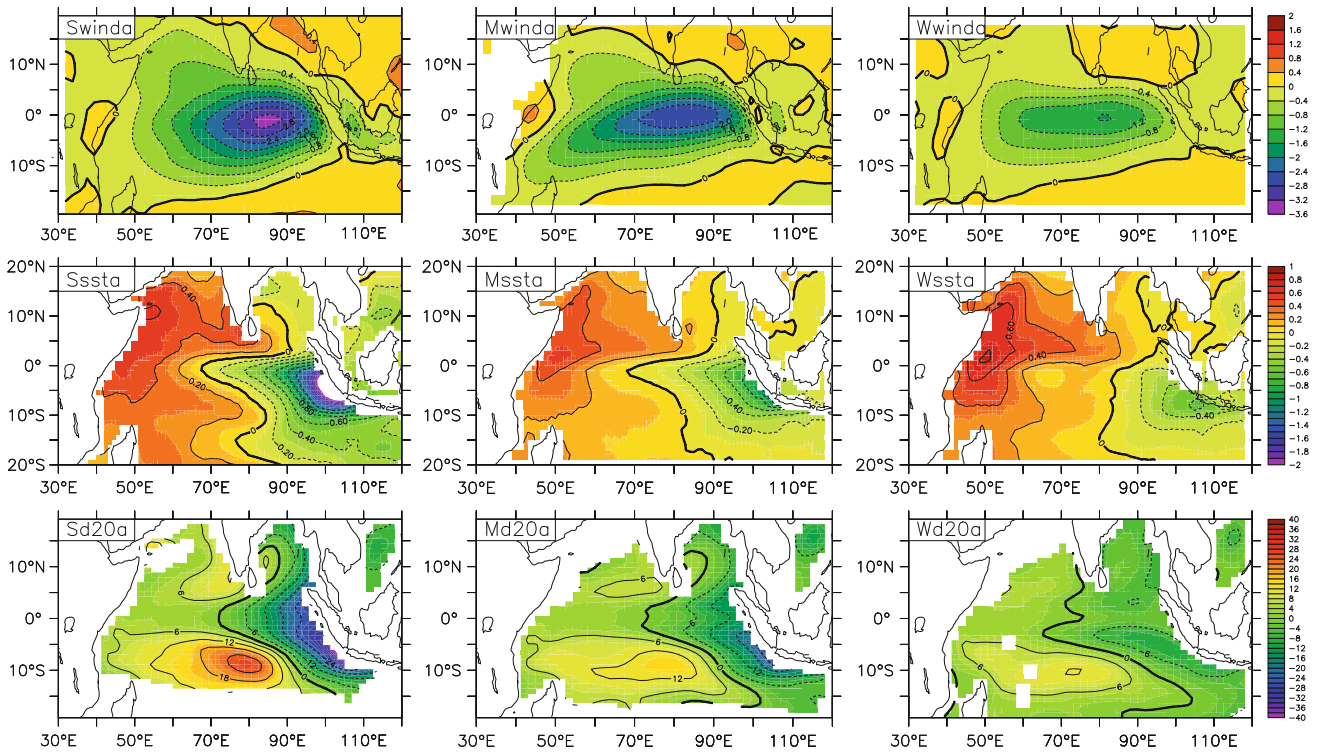

Fig. 3 Composites maps of anomalous surface zonal wind (*top*, unit: m s^{-1}), SST (*middle*, unit: K) and 20 °C isothermal depth (*bottom*, unit: m) fields in SON for the strong (*left*), moderate (*middle*) and weak (*right*) model groups

heat flux anomaly is in response to a unit SSTA change. Thus it reflects the strength of the thermodynamic air-sea feedback. The first term in the right hand side of Eq. (1) represents the vertical advection of anomalous subsurface temperature by the mean upwelling velocity, thus reflecting the strength of the Bjerknes dynamic air-sea feedback. We hereby define the first term in the right hand side of Eq. (1) as the Bjerknes feedback intensity index (BFI) and the second term as the thermodynamic feedback intensity index (TFI) (Liu et al. 2011), which will be analyzed in the following. The BFI may be written as:

$$BFI = \rho C_w \bar{w} R(u,T) R(D,u) R(Te,D) \quad (2)$$

Equation (2) states that the BFI depends on the mean vertical velocity and a product of the SST-wind, wind-thermocline and thermocline-subsurface temperature coupling coefficients during the IOD developing phase. It measures the overall strength of the Bjerknes feedback in each model. Figure 7 shows the averaged values of the SST-wind, wind-thermocline and thermocline-subsurface temperature coupling coefficients and BFI respectively for the strong, moderate and weak composites. For comparison, the observed coupling coefficients and BFI are also shown in the figure.

The above analysis points to the important role of the dynamic air-sea coupling in determining the strength of the model IODs. Saji et al. (2006) performed the research on the relationship between the STD of DMI and the mean thermocline depth off Java (see their Fig. 13a). They showed that there is a weak tendency for a larger DMI variance to occur in a model with a shallower mean thermocline off Java, but the scatter is quite large, with the exclusion of two outlier models. The complicated relationship implies that the intensity of the IOD is not simply determined by the Bjerknes feedback and other processes may also play a role in determining the IOD intensity. Given that the IOD is also affected by the thermodynamic air-sea coupling, in the following we will examine the wind-evaporation-SST feedback and the cloud-radiation-SST feedback in the SEIO.

4.2 Thermodynamic air-sea feedback

Two types of thermodynamic air-sea feedback processes are involved during the IOD developing phase (Li et al. 2002, 2003). One is a positive feedback among the SST, surface wind, and evaporation. The positive feedback is due to the background southeasterly winds in the SEIO, under which an anomalous southeasterly induced by a cold SSTA may further enhance the cold SSTA through increasing surface evaporation. Another is a negative feedback among the SST, cloud, and shortwave radiation anomalies, that is, a cold SSTA leads to the decrease of clouds, which further increases the downward shortwave

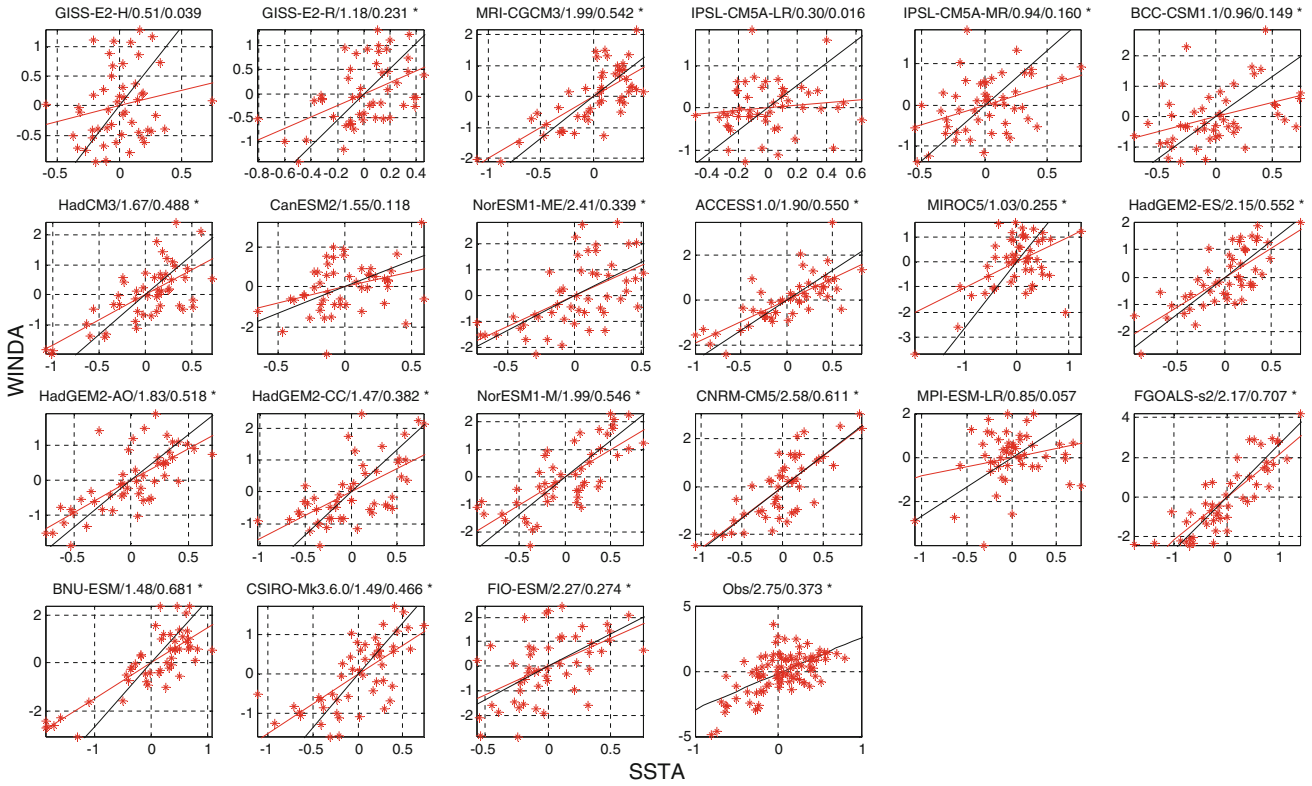

Fig. 4 Scatter diagrams revealing relationships between surface zonal wind anomaly (*vertical axis*, unit: m s^{-1}) in the CEIO and SSTA (*horizontal axis*, unit: K) in the SEIO during the IOD developing phase (JAS) for each of 21 models (*red*). At *each panel*, the name of each model is shown in the *top*, and the numbers at the *top* indicate the slope of each *fitted line* and R^2 between variables, the *black line* indicates the *fitted line* from observation, the *asterisks* indicates the model with significant relationship

radiation and suppresses the development of cold SSTA. This negative feedback is extremely asymmetric, which had been reported by previous studies (Hong et al. 2008 and Cai et al. 2012).

How well do the CMIP5 models simulate such a positive WES feedback? To quantitatively measure the feedback strength, we plot the scatter diagram (Fig. 8) to illustrate the relationship between the surface latent heat flux (LHF) anomaly and the SSTA in the SEIO on June–July–August (JJA) season. For comparison, the observed counterpart is also plotted.

We hereby denote R(LHF, T) to represent the WES feedback coefficient, which can be measured by the slope at each panel of Fig. 8. The observed feedback coefficient is 4.17 W m^{-2} K^{-1}. This amount of anomalous heat flux could be used to further enhance the local SST cooling. Many CMIP5 models (including these in the strong simulation group) fail to reproduce such a positive feedback process. The further study illustrates the unrealistic simulated latent heat flux feedback is due to the incorrect simulation of the surface wind speed field in the individual models. The result is similar with the CMIP3 coupled models (Liu et al. 2011). The large bias in the WES feedback poses a great challenge to many state-of-art CGCMs.

To examine the cloud-radiation-SST feedback among the 21 models, we show the simultaneous relationship between the shortwave radiation and SST anomalies averaged in JAS over the SEIO (Fig. 9). Different from the positive WES feedback, a negative feedback between the observed SST and shortwave radiation anomalies exists in the SEIO. While most of the coupled models reproduce such a negative feedback process, HadCM3 model, surprisingly, exhibits a weak positive feedback.

We denote R(SWR, T) to measure the strength of the negative cloud-radiation-SST feedback. The averaged slope of the strong composite is −19 W m^{-2} K^{-1}, which is about twice as large as that (−7.4 W m^{-2} K^{-1}) in the weak composite.

The overall thermodynamic feedback intensity (TFI) may be measured by the sum of the WES feedback and the cloud-radiation-SST feedback, that is,

$$TFI = R(LHF, T) + R(SWR, T) \quad (3)$$

Figure 10 shows the diagrams of R(LHF, T), R(SWR, T) and TFI for the strong, moderate and weak composites and for the observation. The major bias appears in the latent heat flux-SST relationship. Consequently, the overall

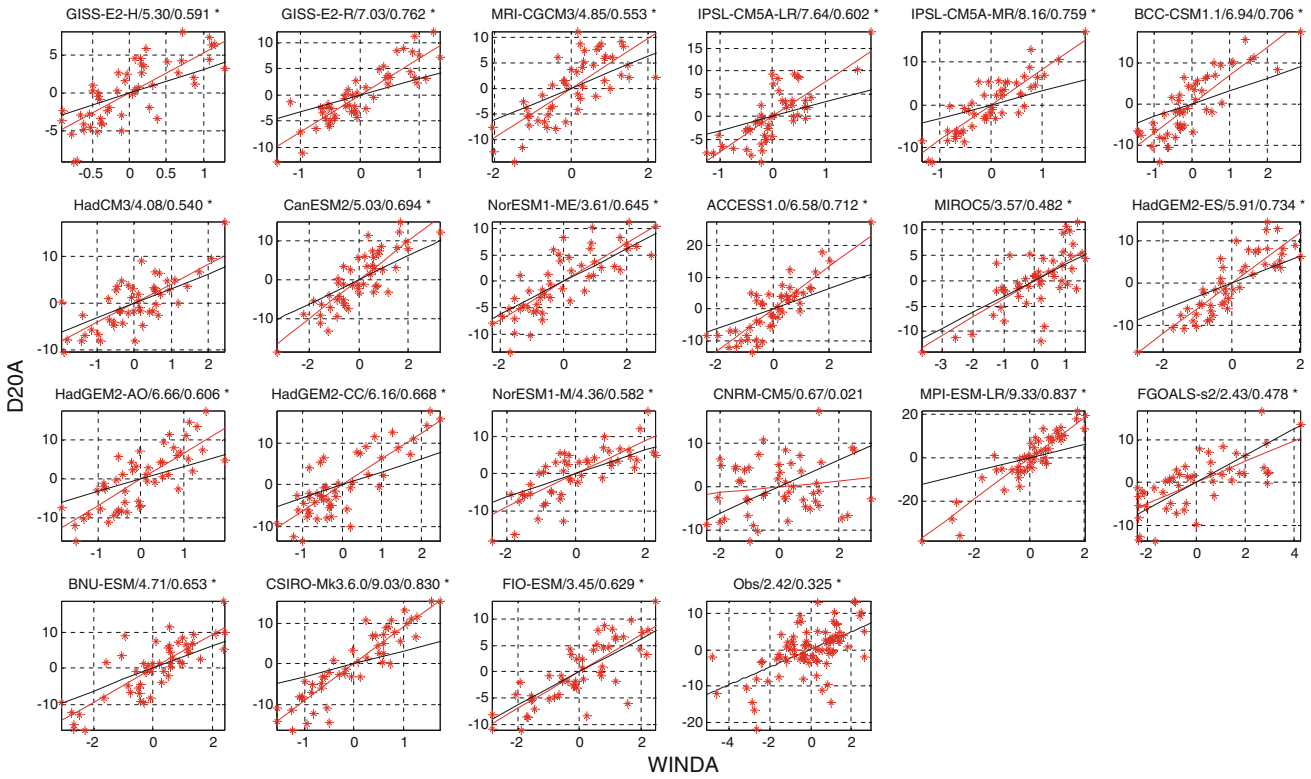

Fig. 5 Same as in Fig. 4 except for the relationship between the thermocline depth anomaly (*vertical axis*, unit: m) in the SEIO and the surface zonal wind anomaly (*horizontal axis*, unit: m s^{-1}) in the CEIO

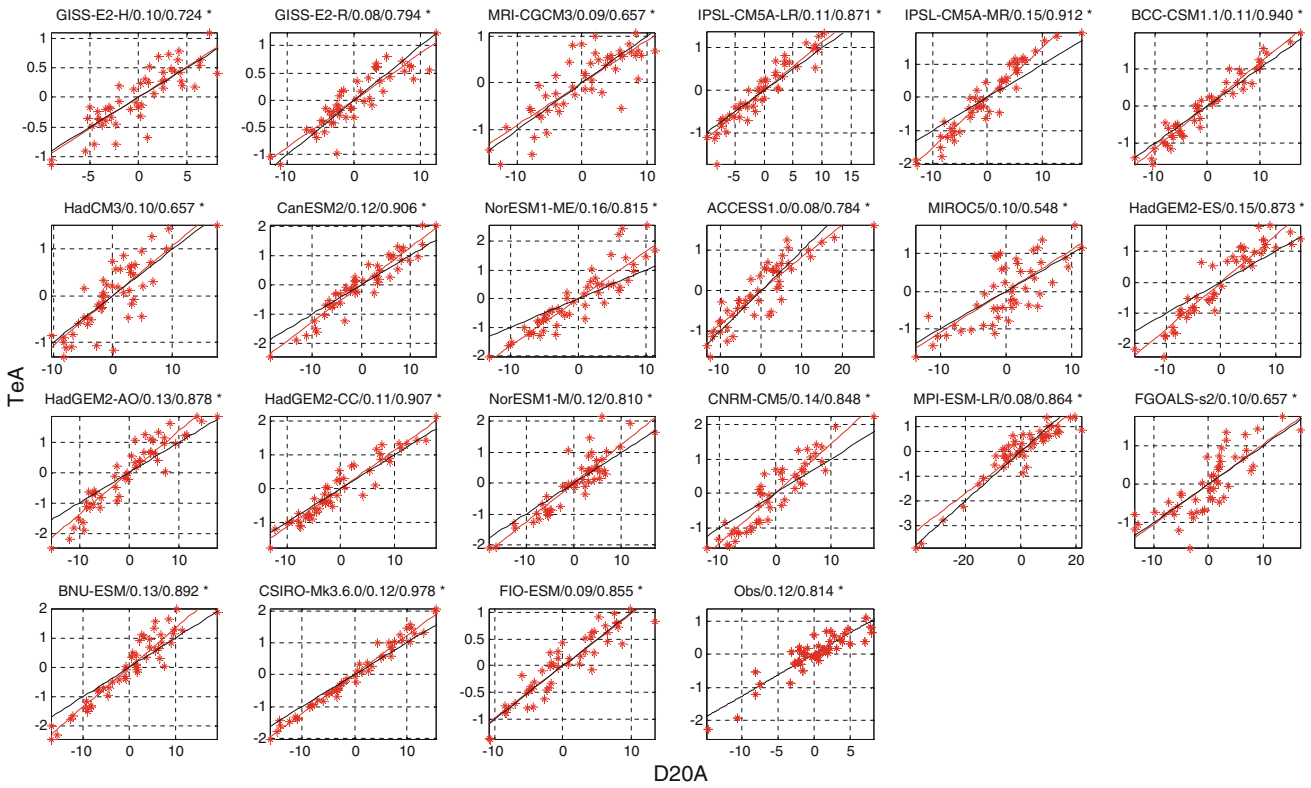

Fig. 6 Same as in Fig. 4 except for the relationship between the subsurface temperature anomaly at 70 m (*vertical axis*, unit: K) and the thermocline depth anomaly (*horizontal axis*, unit: m) in the SEIO

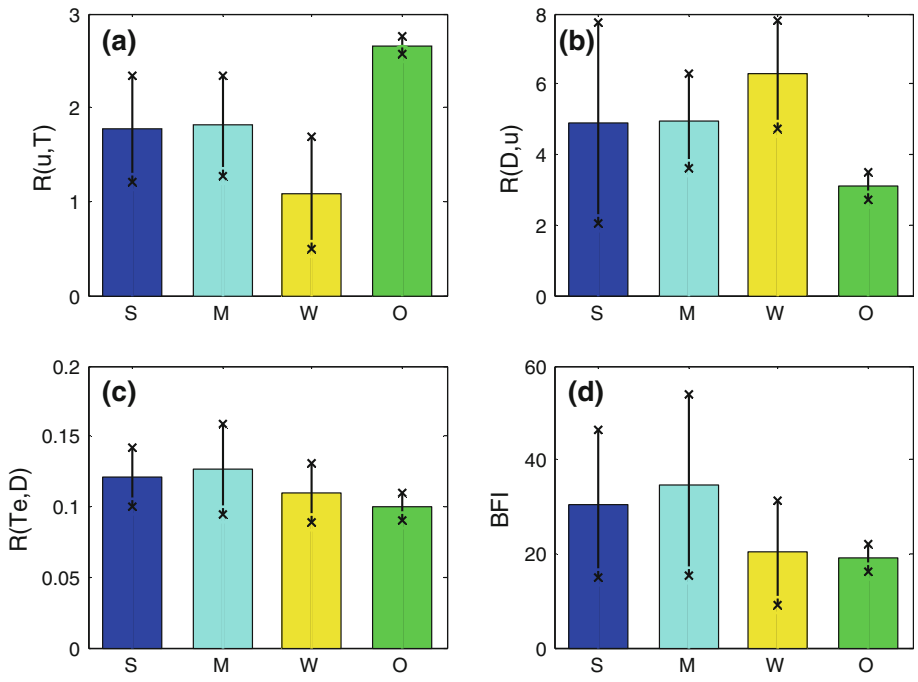

Fig. 7 R(u,T) (unit: m s^{-1} k^{-1}), R(D,u) (unit: m per m s^{-1}), R(Te,D) (unit: K m^{-1}) and BFI (unit: W m^{-2} K^{-1}) in JAS season for the strong (denoted by '*S*'), moderate (denoted by '*M*'), and weak (denoted by '*W*') composites and from the observational data (denoted by '*O*'). *Error bars* indicate the strength spread among different groups

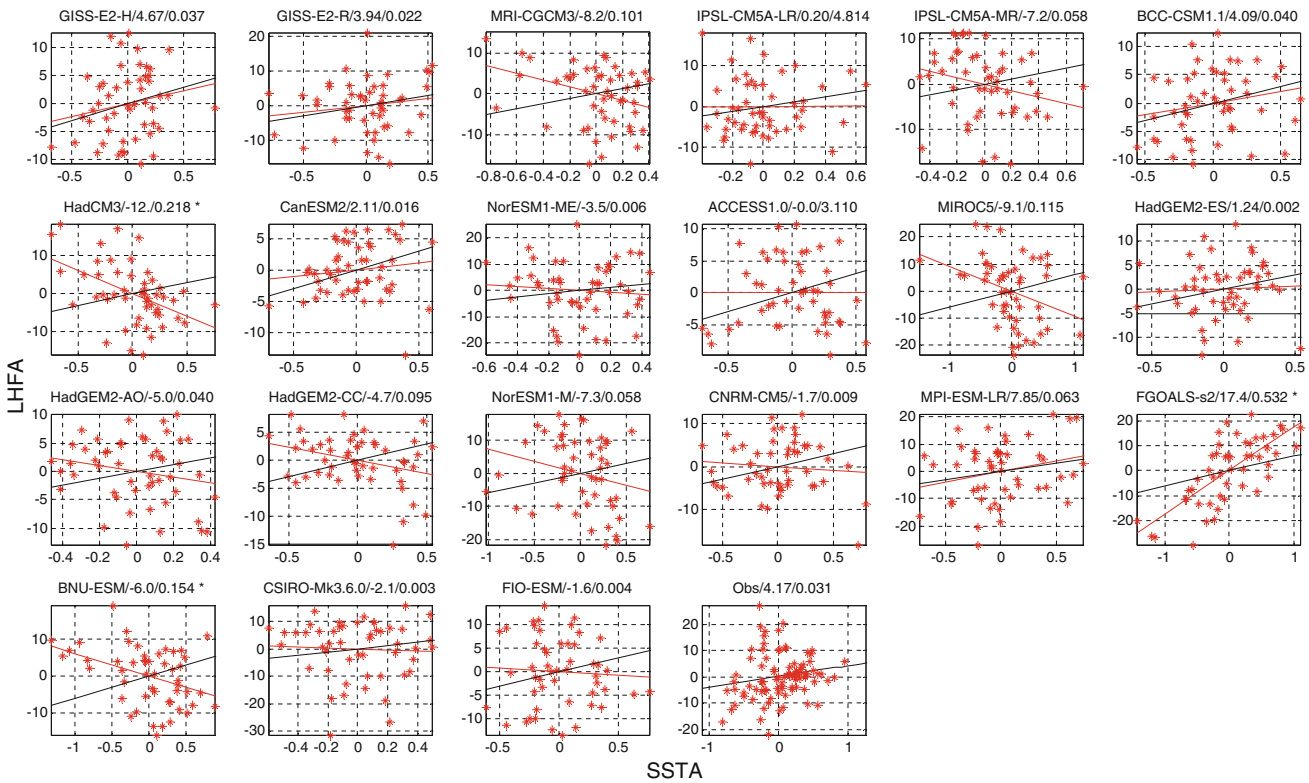

Fig. 8 Similar as in Fig. 4 except for the relationship between the surface latent heat flux anomaly (*vertical axis*, unit: W m^{-2}) and SSTA (*horizontal axis*, unit: K) in the SEIO on JJA season. The latent heat flux is defined positive downward

thermodynamic damping in all the three groups is overestimated, compared to the observation. The strongest (weakest) thermodynamic damping appears in the moderate (weak) group.

4.3 Combined feedback

The diagnosis above reveals that greater (weaker) Bjerknes and thermodynamic feedbacks co-exist in the strong

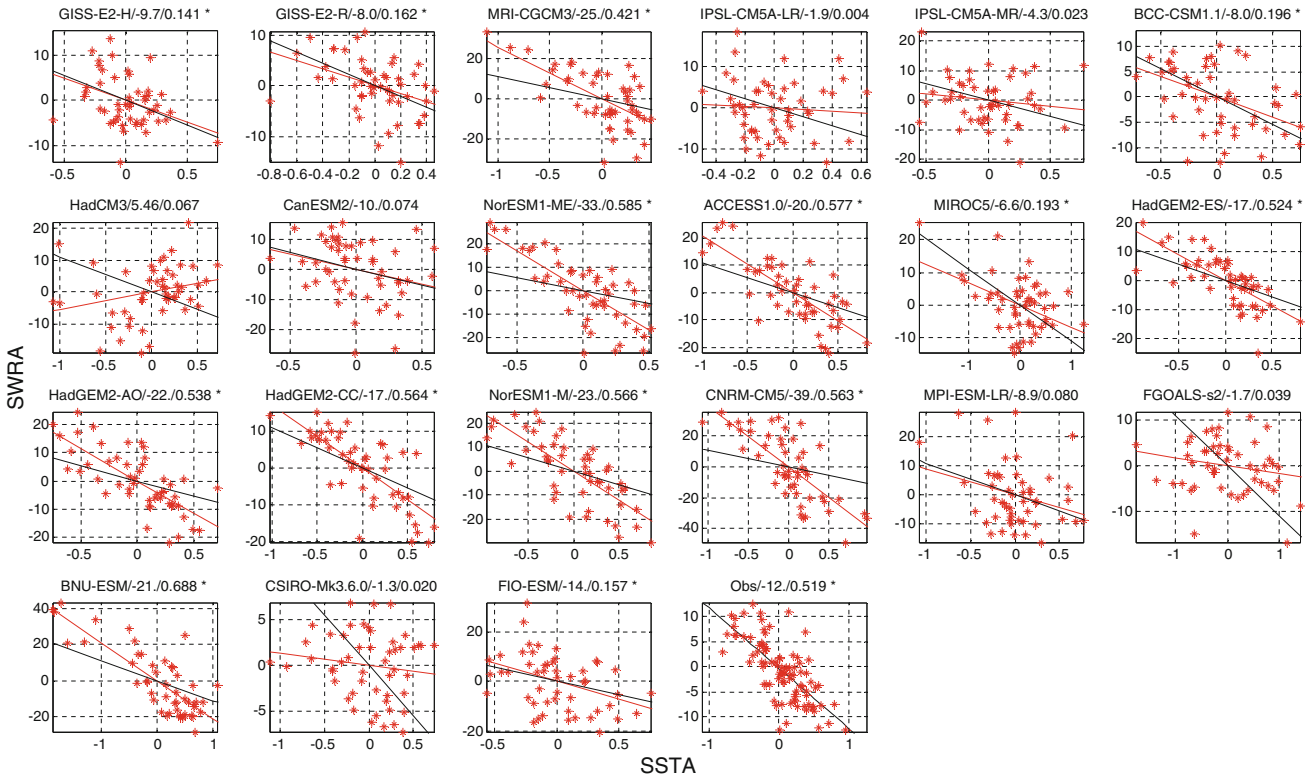

Fig. 9 Same as in Fig. 4 except for the relationship between the surface net shortwave radiation anomaly (*vertical axis*, unit: W m^{-2}) and SSTA (*horizontal axis*, unit: K) in the SEIO

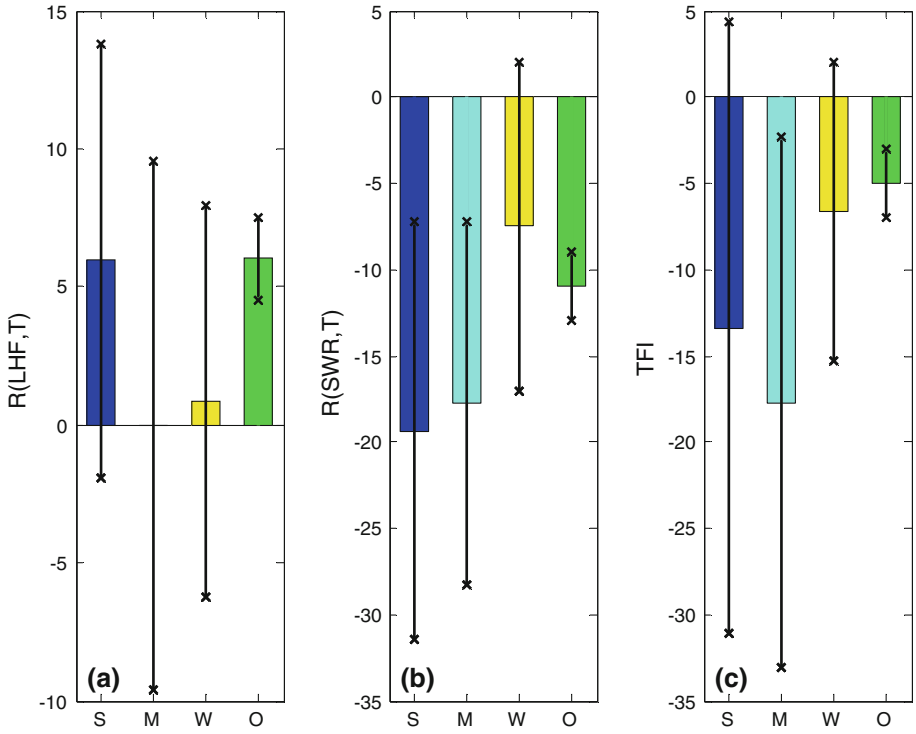

Fig. 10 R(LHF,T), R(SWR,T) and TFI (unit: W m^{-2} K^{-1}) averaged during JAS season for the strong, moderate and weak composites (denoted as '*S*', '*M*' and '*W*' respectively) and from the observation (denoted as '*O*'). *Error bars* indicate the strength spread among different groups

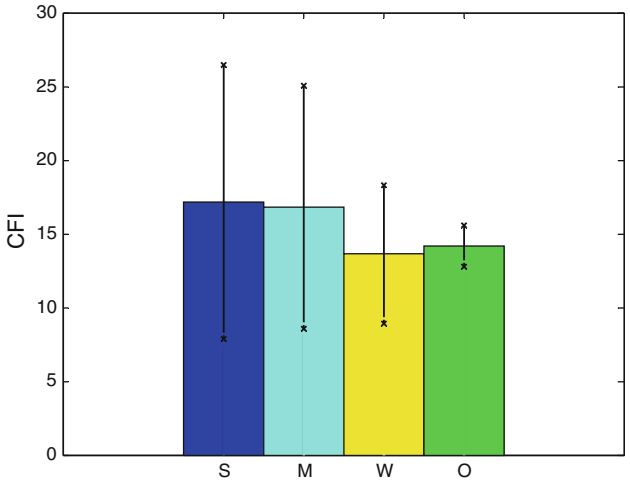

Fig. 11 The combined Bjerknes and thermodynamic feedback intensity index (CFI (unit: W m^{-2} K^{-1})) during the IOD developing phase (JAS) for the strong ('*S*'), moderate ('*M*') and weak ('*W*') composites and from the observation ('*O*'). *Error bars* indicate the strength spread among different groups

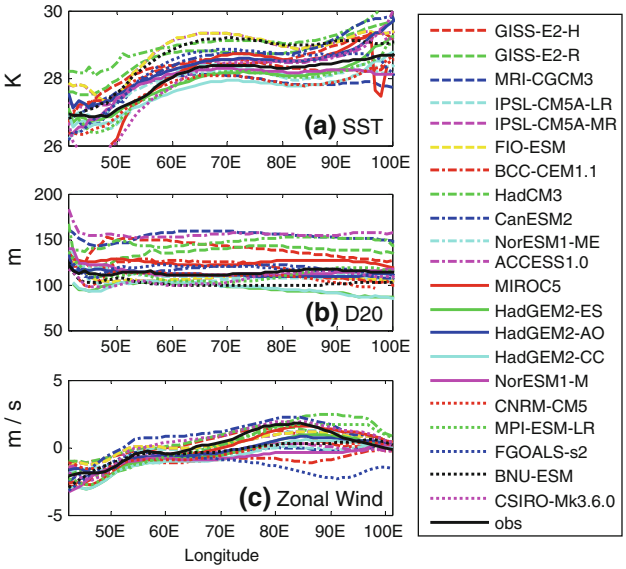

Fig. 12 The mean SST (*upper*, unit: K), thermocline depth (*middle*, unit: m) and the sea surface zonal wind (*lower*, unit: m s^{-1}) along the equatorial IO averaged from observation and each CMIP5 models

(weak) model group. Thus, it is necessary to examine the combined dynamical and thermodynamic feedback processes. Define a combined dynamic and thermodynamic feedback intensity index (CFI) as below:

$$CFI = BFI + TFI \tag{4}$$

Figure 11 illustrates the averaged CFI for the strong, moderate and weak groups. For comparison, the observed CFI is also shown. The CFI values in the three groups well reflect the simulated IOD strength, that is, the greater the CFI, the stronger the overall dynamic and thermodynamic coupling strength, and the greater the model IOD intensity.

5 Differences in the coupled model mean state

Why do some CMIP5 models produce strong dynamic and thermodynamic coupling on the interannual timescale while others do not? As the interannual anomalies evolve under the background mean state, it is necessary to examine the difference in the mean climate state among the coupled models.

From Fig. 12, the simulated SSTs in 21 models are nearly uniform east of 60°E within a range of 27.5–29.5 °C, and relative cool in the west off Africa. With a few exceptions, mean winds are weak in the equator, generally less than 2 m s^{-1}. Thermocline spatial distribution is quite similar to the observation. Overall, the models show high skill in simulating the zonal distributions of SST and thermocline depth along the equator.

A deep background thermocline implies a weak Bjerknes feedback strength. This partly accounts for the fact that the SSTA associated with El Niño grows much faster in the eastern equatorial Pacific than in the western equatorial Pacific. Figure 12 shows the simulated mean thermocline depth along the equatorial IO in the CMIP5 models. Note that the averaged annual mean thermocline depth in the strong composite is 110 m, with a small annual variation, while the mean thermocline depth is 150 m for the weak composite (Fig. 13). This remarkable mean thermocline depth difference may contribute to the difference in the Bjerknes feedback intensity between the strong and weak groups (Li and Xie 2012).

6 Discussion

Although most CMIP5 coupled models simulate the IOD mode and relevant dynamic and thermodynamic feedback processes in the tropical IO, unrealistic simulations exist among these models. The negative shortwave radiation-SST feedback is the important thermodynamic air-sea coupling process that could impact the IOD strength, which can be well captured by most of the CMIP5 models. However, the HadCM3 model fails to reproduce the observed feature.

To understand the cause of the unrealistic simulation of the shortwave radiation during the IOD developing phase, we show the composite maps of the SST and cloud cover anomalies in Fig. 14. Here the composite is made based on R(SWR, T) > 0 model. In the observation, in response to a negative SSTA in the SEIO, the local cloud cover anomaly is negative (Liu et al. 2011), implying that local convection is suppressed and more shortwave radiation may reach the

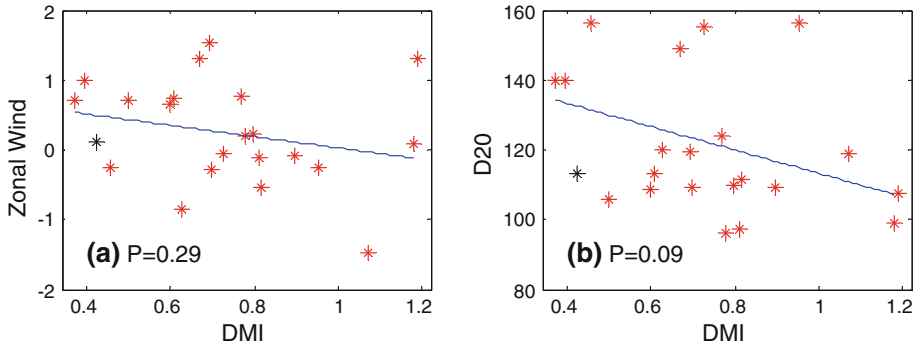

Fig. 13 Scatter diagrams revealing relationships between IOD strength and mean surface zonal wind (**a**) and the thermocline depth (**b**) along the Indian Ocean equator for each of the 21 models (*red*) and the observation (*black*). *P* values are listed in each diagram. The slope is −0.81 for (**a**) and −33.5 for (**b**)

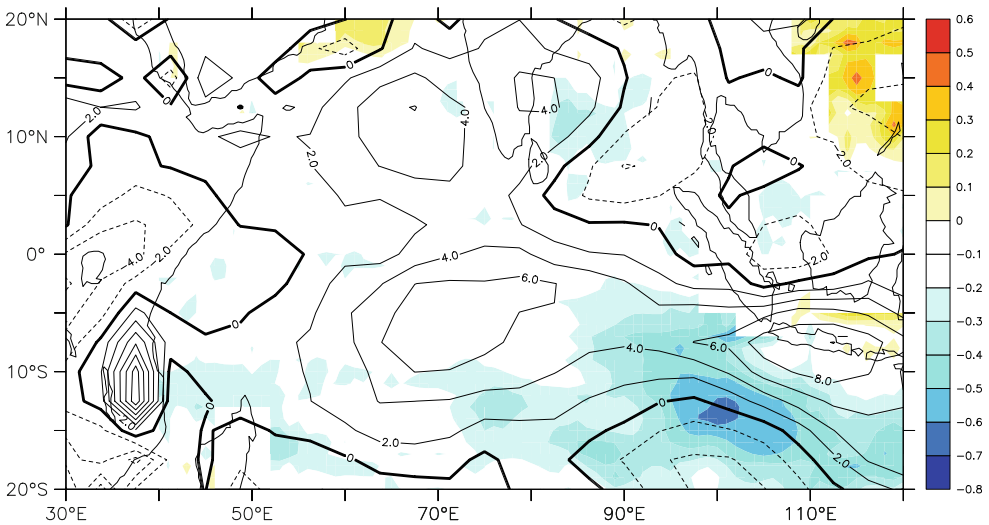

Fig. 14 Composite maps of the SSTA (*shading*, unit: K) and cloud cover fraction (contour) anomalies during the IOD developing phase (JAS) from the positive R(SWR,T) model composite. The composite was made based on the most significant positive R(SWR,T) events over a negative SSTA in the SEIO (90°E–110°E, 0–10°S)

ocean surface to damp the cold SSTA. Similar to the observation, negative R(SWR, T) models well capture a negative cloud cover anomaly over the SEIO (Figure not shown). It is interesting to note that the positive R(SWR, T) model composite shows a positive cloud cover anomaly right above the cold SSTA in the SEIO, and a negative cloud cover anomaly appears to be shifted to its west. This unrealistic anomalous cloud pattern implies a positive rather than a negative shortwave radiation-SST feedback. The analysis demonstrates that apparently there is a bias in cloud fraction calculation in HadCM3 models, which might lead to the unrealistic cloud-SST feedback over the region. Except for the unrealistic simulated cloud, the R(SWR, T) asymmetry in positive and negative IOD event may also contribute to such unrealistic simulation (Hong et al. 2008; Cai et al. 2012).

The results above point to possible biases in the thermodynamic air-sea coupling in some of current state-of-art CGCMs. The comparison of overall performance of the IOD simulations among the 21 models suggests that the most serious problem lies in the thermodynamic air-sea coupling. As most of these CGCMs are also used for future climate projection, caution is needed in interpreting the model generated global and regional SST changes.

Figure 15 compares the simulated dynamical and thermodynamic feedback strength in CMIP3, CMIP5 and observations separately. Compared to CMIP3, the CMIP5 ensemble reproduces the simulation of Bjerknes dynamic feedback is apart from observation, in particular with regarding to the wind response to SST forcing and worse thermocline response to surface wind forcing. For part of the wind response to SST forcing, all modeling centers present weaker simulated feedback strength than observation associated with large spread among models and five of them (GISS, IAP, IPSL, MPI, MRI) present weaker simulation than CMIP3 (Fig. 15c). Figure 15d illustrates the tendency for most models to present stronger thermocline response to wind forcing from CMIP5 to CMIP3 except for two modeling centers (CNRM, and MIROC). Figure 15e indicates the third part of Bjerknes feedback in CMIP5 present stronger strength than both CMIP3 and observation, where only two modeling centers show weaker simulation (MPI, and MRI). In general, the responses from three dynamic

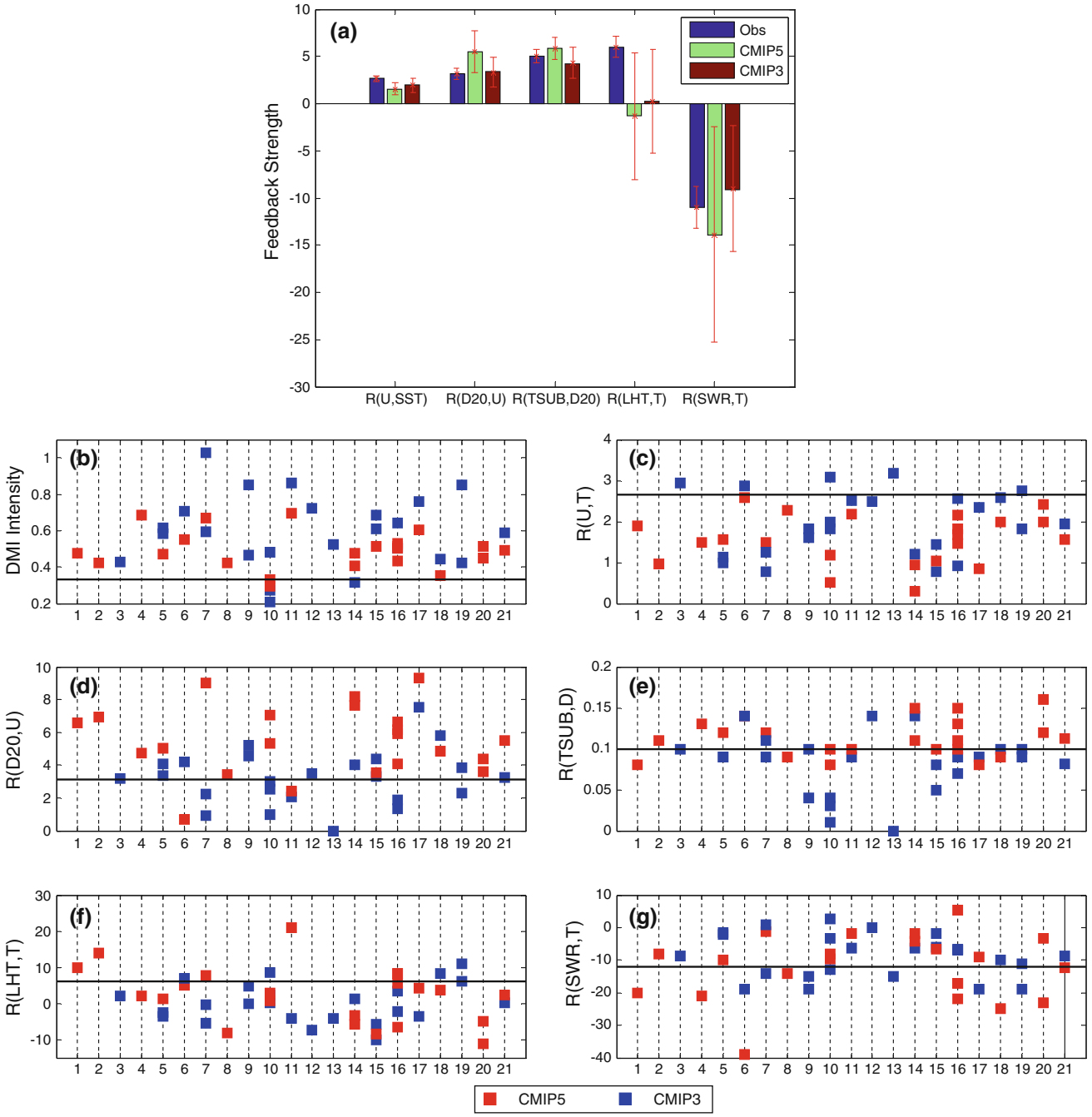

Fig. 15 **a** R(U,SST), R(D20,U), R(TSUB, D20), R(LHF,T) and R(SWR,T) averaged during JAS season for the observation, CMIP3 and CMIP5 composites (denoted as '*obs*', '*CMIP3*' and '*CMIP5*' respectively). The *error bars* indicate the model spread among CMIP3 and CMIP5 models. **b–f** Similar as (**a**) but with the simulated strength of IOD intensity (**b**), R(U,SST) (**b**), R(D20,U) (**c**), R(TSUB, D20) (**d**), R(LHF,T) (**f**) and R(SWR,T) (**g**) of individual model for CMIP3 (*blue*), CMIP5 (*red*) in the same modeling centers, and the observation (*black solid line* in (**b**)–(**f**)). For (**b**)–(**f**), the *horizontal axis* present different modeling centers: *1* ACC, *2* BCCR, *3* BCC, *4* BNU, *5* CCCMA, *6* CNRM, *7* CSIRO, *8* FIO, *9* GFDL, *10* GISS, *11* IAP, *12* INGV, *13* INM, *14* IPSL, *15* MIROC, *16* MOHC, *17* MPI, *18* MRI, *19* NCAR, *20* NCC, *21* ensemble mean of CMIP3 and CMIP5

feedbacks strength have not improved for CMIP5, while WES feedback is closer to observation than in CMIP3 (Fig. 15e). For WES feedback simulations, most models can not present the correct tendency as observation both in CMIP3 and CMIP5. The shortwave radiation-SST feedback in CMIP5 is stronger than observations and CMIP3 (Fig. 15f). Regarding feedback processes, CMIP5 has not improved much over CMIP3.

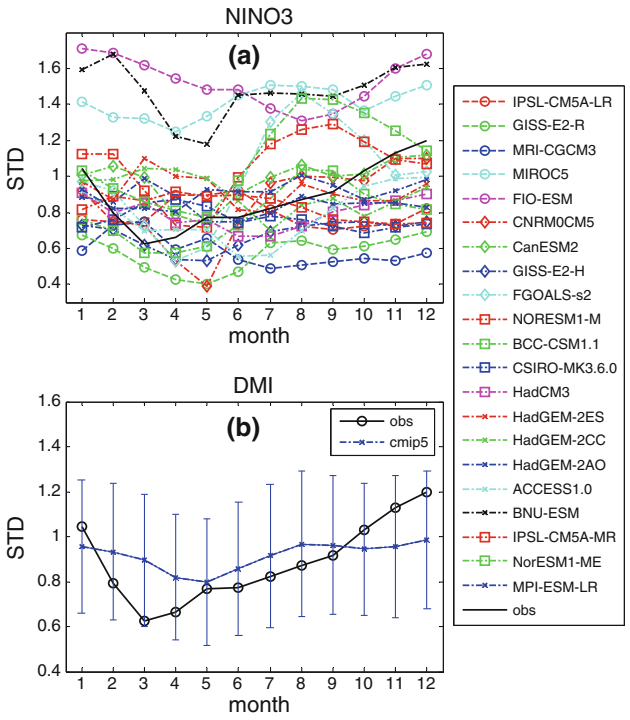

Fig. 16 Monthly standard deviations of NINO3 index from 21 CMIP5 coupled models and the observation (**a**, unit: K) and the monthly standard deviations of DMI from 21 CMIP5 models (*cmip5*) and the observation (*obs*) (**b**, unit: K). The *error bar* indicates the standard deviation spread among coupled models

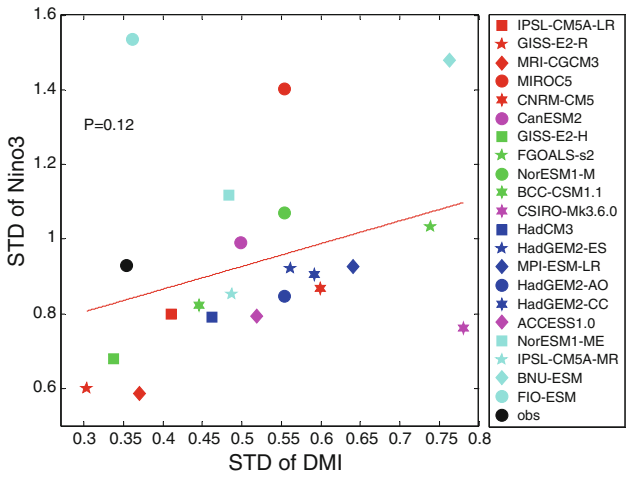

Fig. 17 Scatter diagram revealing relationships between IOD strength and ENSO strength, defined by STD of each index, for the observation and each of the CMIP5 coupled models

In addition to the dynamic and thermodynamic feedback processes in the tropical Indian Ocean, the remote forcing from ENSO over the tropical Pacific influences IOD in coupled models (Cai et al. 2011). Figure 16 shows the monthly STD distribution of an ENSO index for CMIP5 simulations and observations. Bellenger et al. 2013 had performed the detailed analysis on the ENSO simulation between CMIP3 and CMIP5. The simulated ENSO among CMIP5 coupled models presents great diversity in amplitude as well as phase locking. The ensemble averaged ENSO strength is weaker than in observations during the ENSO peak season. 7 of 21 models give stronger ENSO than observations. Most CMIP5 models show stronger IOD amplitude at the developing and peak seasons. Although the CMIP5 models present distinct performance between the IOD and ENSO simulation, these two interannual modes are closely connected. Figure 17 compares IOD and ENSO amplitudes in observation and CMIP5 models. Except for the CSIRO-MK3.6.0 model, which suffers from large biases in IOD simulation, the IOD amplitude shows a tendency to increase with ENSO variance, a relationship not found in CMIP3 models (Saji et al. 2006; Cai et al. 2011). The relationship between simulated IOD and ENSO amplitudes is more robust when excluding models with DMI larger than 0.6, which had been pointed by Hong et al. (2008). It is worthy of mention that the strength of Indian Ocean Basin Mode (IOB), a basin-wide warming takes place over the tropical Indian Ocean, peaks in late boreal winter and early spring, and persists through boreal summer, is highly correlated with the ENSO amplitude in CMIP5, not only in each individual model but also across the models, suggest a closely relationship between tropical Pacific and Indian Ocean climate (Du et al. 2013b).

ENSO can affect IOD through the atmosphere bridge and the ocean pathway (Cai et al. 2011). El Niño induced easterly wind anomalies over the equatorial Indian Ocean. During May–October, these wind anomalies lead to a thermocline shoaling off Java-Sumatra. This then triggers a fast growth of the IOD through Bjerknes feedback (Saji et al. 1999). Additionally, the easterly anomalies superimpose onto the climatological southeasterly flow to generate heat flux anomalies conducive for a rapid growth of the cooling anomaly in the southeastern equatorial Indian Ocean (Hendon 2003). ENSO signals propagate into the Indian Ocean through oceanic teleconnections, arriving at the northwest Australia coast and then radiating into the interior Indian Ocean (Wijffels and Meyers 2004; Cai et al. 2005; Shi et al. 2007). On decadal or longer time scales, this teleconnection process can change the background state of the thermocline in the equatorial and eastern Indian Ocean (Shi et al. 2008), hence the properties of IOD. Recent study indicates that mean state changes modulate IOD in a warmer climate through the change of thermocline feedback and atmosphere feedback (Zheng et al. 2013).

7 Summary and conclusion

The Indian Ocean Dipole is one of dominant modes in the tropical IO on the interannual timescale. This study shows

that the simulated IOD in CMIP5 has not improved much compared to CMIP3. Although the ensemble averaged IOD strength in CMIP5 is closer to observations. In this study we evaluate the performance of 21 WCRP CMIP5 models in IOD simulation, by examining the dynamical and thermodynamic air-sea coupling processes.

Based on the IOD amplitude, the 21 coupled models are classified into strong, moderate and weak IOD simulation groups. The composite analysis is further conducted to reveal common features and differences among the strong and weak groups.

To study the cause of the diversity in the model IOD intensity, we first examine the Bjerknes feedback. This dynamic ocean–atmosphere feedback consists of the following three key processes: (1) how strongly the atmospheric low-level wind responds to one unit SSTA forcing, (2) how strongly the ocean thermocline depth responds to one unit surface wind forcing, and (3) how strongly the ocean subsurface temperature responds to one unit thermocline depth variation. These three dynamical feedback processes are examined and the respective coupling coefficients are estimated in all the 21 models. The overall strength of the Bjerknes dynamic feedback is determined by the product of the three coupling coefficients and the mean upwelling velocity. The comparison of the strong and weak composites shows that the former attains a much greater Bjerknes feedback intensity than the latter.

Next we examine the thermodynamic air-sea coupling strength for all the 21 models. Two thermodynamic air-sea feedback processes, WES feedback and the cloud-radiation-SST feedback, are examined. While observations show a positive feedback among the wind, evaporation (or surface latent heat flux) and SST during the IOD developing phase (Li et al. 2003), about a half of the CMIP5 models failed to capture this thermodynamic air-sea feedback. As a strong negative feedback process, the cloud-radiation-SST feedback may slow down the IOD development. Most of the CMIP5 models successfully simulated this negative feedback process, even though the feedback intensity varies among the models. The averaged negative feedback coefficient is greater (smaller) in the strong (weak) composite than observation, implying a stronger (weaker) thermodynamic damping.

The CMIP5 ensemble produces a more realistic positive WES feedback during the IOD developing phase, while it produces a worse Bjerknes dynamic feedback than CMIP3. The lack in improvement from CMIP3 to CMIP5 is most noticeable in the wind response to SST forcing which is underestimated in the newer generation models while the thermocline response to surface wind forcing is overestimated. The overall CMIP5 performance in the IOD simulation does not show remarkable improvement compared to the CMIP3 simulations.

The distinctive features in the dynamic and thermodynamic coupling between the strong and weak composite are closely related to the difference in the coupled model mean state. The comparison of the strong and weak composites shows that there are remarkable differences in the mean thermocline depth. The models with a deeper mean thermocline are often associated with weaker dynamic coupling strength and a weak IOD signal.

In this study we have found the detailed dynamic and thermodynamic air-sea feedback processes in 21 CMIP5 models and showed their possible roles in the diversity of IOD simulations in relation to the model mean state. We performed a preliminary analysis on the relationship between ENSO and IOD, suggesting that the IOD amplitude is proportional to the ENSO variance, if a model generates a strong ENSO, it is likely that this model also simulates a strong IOD.

Acknowledgments We acknowledge the World Climate Research Programme's Working Group on Coupled Modelling, which is responsible for CMIP, and we thank the climate modeling groups for producing and making available their model output. For CMIP the U.S. Department of Energy's Program for Climate Model Diagnosis and Intercomparison provides coordinating support and led development of software infrastructure in partnership with the Global Organization for Earth System Science Portals. We wish to thank L. X. Xu and L. Feng for data preparation. This work was supported by Chinese National Basic Research Program grants: 2010CB950304, 2012CB955601 and ARCP2013-27NSY-Liu grants and the Natural Science Foundation of China (41376037, 41306030, and 41106010).

References

Ashok K, Guan Z, Saji NH, Yamagata T (2004) Individual and combined influences of ENSO and Indian Ocean dipole on the Indian summer monsoon. J Clim 17:3141–3155

Behera SK, Luo JJ, Masson S, Delecluse P, Gualdi S, Navarra A (2005) Paramount impact of the Indian Ocean dipole on the east African short rains: a CGCM study. J Clim 18:4514–4530

Bellenger H, Guilyardi E, Leloup J, Lengaigne M, Vialard J (2013) ENSO representation in climate models: from CMIP3 to CMIP5. Clim Dyn. doi:10.1007/s00382-013-1783-z

Bjerknes J (1966) A possible response of the atmospheric Hadley circulation to equatorial anomalies of ocean temperature. Tellus 18:820–829

Bjerknes J (1969) Atmospheric teleconnections from the equatorial Pacific. Mon Weather Rev 97:163–172

Cai W, Cowan T (2013) Why is the amplitude of the Indian Ocean Dipole overly large in CMIP3 and CMIP5 climate models? Geophys Res Lett 40:1200–1205. doi:10.1002/grl.50208

Cai W, Qiu Y (2013) An observation-based assessment of nonlinear feedback processes associated with the Indian Ocean Dipole. J Clim 26:2880–2890

Cai WJ, Hendon HH, Meyers G (2005) Indian Ocean dipole like variability in the CSIRO Mark 3 coupled climate model. J Clim 18:1449–1468

Cai W, Sullivan A, Cowan T (2011) Interactions of ENSO, the IOD, and the SAM in CMIP3 Models. J Clim 24:1688–1704

Cai W, Rensch PV, Cowan T, Hendon HH (2012) An asymmetry in the IOD and ENSO teleconnection pathway and its impact on Australian climate. J Clim 25:6318–6329

Carton JA, Chepurin G, Cao X, Giese B (2000) A simple ocean data assimilation analysis of the global upper ocean 1950–95. Part I: methodology. J Phys Oceanogr 30:294–309

Du Y, Qu T, Meyers G, Masumoto Y, Sasaki H (2005) Seasonal heat budget in the mixed layer of the southeastern tropical Indian Ocean in a high-resolution ocean general circulation model. J Geophys Res 110:C04012. doi:10.1029/2004JC002845

Du Y, Qu T, Meyers G (2008) Interannual variability of the sea surface temperature off Java and Sumatra in a global GCM. J Clim 21:2451–2465

Du Y, Cai W, Wu Y (2013a) A new type of the Indian Ocean Dipole since the mid-1970s. J Clim 26:959–972

Du Y, Xie S-P, Yang Y, Zheng X-T, Liu L, Huang G (2013b) Indian Ocean variability in the CMIP5 multi-model ensemble: the basin mode. J Clim. doi:10.1175/JCLI-D-12-00678.1

England MH, Ummenhofer CC, Santoso A (2006) Interannual rainfall extremes over Southwest Western Australia linked to Indian Ocean climate variability. J Clim 19:1948–1969

Gill AE (1980) Some simple solutions for heat-induced tropical circulation. Q J R Meteorol Soc 106:447–462

Hendon H (2003) Indonesian rainfall variability: impacts of ENSO and local air–sea interaction. J Clim 16:1775–1790

Hong C–C, Li T, Ho L, Kug J-S (2008) Asymmetry of the Indian Ocean Dipole. Part I: observational analysis. J Clim 21:4834–4848

Ishii M, Kimoto M (2009) Reevaluation of historical ocean heat content variations with time-varying XBT and MBT depth bias corrections.J. Oceanography 65(3):287–299

Kistler R, Kalnay E, Collins W, Saha S, White G, Woollen J, Chelliah M, Ebisuzaki W, Kanamitsu M, Kousky V, van den Dool H, Jenne R, Fiorino M (2001) The NCEP-NCAR 50-year reanalysis: monthly means CD-ROM and documentation. Bull Am Meteorol Soc 82:247–268

Li G, Xie S-P (2012) Origins of tropical-wide SST biases in CMIP multi-model ensembles. Geophys Res Lett 39:L22703. doi:10.1029/2012GL053777

Li T, Zhang YS, Lu E, Wang D (2002) Relative role of dynamic and thermodynamic processes in the development of the Indian Ocean dipole. Geophy Res Let 29:2110–2113

Li T, Wang B, Chang C-P, Zhang Y (2003) A theory for the Indian Ocean dipole-zonal mode. J Atmos Sci 60:2119–2135

Lindzen RS, Nigam S (1987) On the role of sea surface temperature gradients in forcing low level winds and convergence in the tropics. J Atmos Sci 44:2418–2436

Liu L, Yu W, Li T (2011) Dynamic and thermodynamic air–sea coupling associated with the Indian Ocean Dipole diagnosed from 23 WCRP CMIP3 models. J Clim 24:4941–4958

Liu L, Feng L, Yu W, Wang HW, Liu YL, Sun SW (2013) The distribution and variability of simulated chlorophyll concentration over the tropical Indian Ocean from five CMIP5 models. J Ocean Univ China 12(2):253–259

Luo J–J, Masson S, Behera S, Yamagata T (2007) Experimental forecasts of the Indian Ocean dipole using a coupled OAGCM. J Clim 20:2178–2190

Luo J–J, Behera S, Masumoto Y, Sakuma H, Yamagata T (2008) Successful prediction of the consecutive IOD in 2006 and 2007. Geophys Res Lett 35:L14S02. doi:10.1029/2007GL032793

Luo J–J, Zhang RC, Behera SK, Masumoto Y, Jin F–F, Lukas R, Yamagata T (2010) Interaction between El Nino and extreme Indian Ocean dipole. J Clim 23:726–742

Meehl GA et al (2009) Decadal prediction. Bull Am Meteorol Soc 90:1467–1485. doi:10.1175/2009BAMS2778.1

Rayner NA, Parker DE, Horton EB, Folland CK, Alexander LV, Rowell DP, Kent EC, Kaplan A (2003) Global analyses of sea surface temperature, sea ice, and night marine air temperature since the late nineteenth century. J Geophys Res 108(D14):4407. doi:10.1029/2002JD002670

Saji NH, Yamagata T (2003a) Possible impacts of Indian Ocean Dipole mode events on global climate. Clim Res 25:151–169

Saji NH, Yamagata T (2003b) Structure of SST and surface wind variability during Indian Ocean dipole mode years: COADS observations. J Clim 16:2735–2751

Saji NH, Goswami BN, Vinayachandran PN, Yamagata T (1999) A dipole mode in the tropical Indian Ocean. Nature 401:360–363

Saji NH, Xie SP, Yamagata T (2006) Tropical Indian Ocean variability in the IPCC twentieth-century climate simulations. J Clim 19:4397–4417

Shi G, Ribbe J, Cai W, Cowan T (2007) Multidecadal variability in the transmission of ENSO signals to the Indian Ocean. Geophys Res Lett 34:L09706. doi:10.1029/2007GL029528

Shi GJ, Cai W, Cowan T, Ribbe J, Rotstayn L, Dix M (2008) Variability and trend of North West Australia rainfall: observations and coupled climate modeling. J Clim 21:2938–2959

Simmons AJ, Gibson JK (2000) The ERA-40 project plan. ERA-40 Project Rep. Series No. 1, ECMWF, p 63

Smith TM, Reynolds RW (2003) Extended reconstruction of global sea surface temperatures based on COADS data (1854–1997). J Clim 16:1495–1510

Song Q, Vecchi GA, Rosati AJ (2007) Indian Ocean variability in the GFDL coupled climate model. J Clim 20:2895–2916

Taylor KE, Stouffer RJ, Meehl GA (2012) An overview of CMIP5 and the experiment design". Bull Am Meteorol Soc 93:485–498. doi:10.1175/BAMS-D-11-00094.1

Wang X, Li CY, Zhou W (2006) Interdecadal variation of the relationship between Indian rainfall and SSTA modes in the Indian Ocean. Int J Climatol 26:595–606

Webster PJ, Moore AM, Loschnigg JP, Leben RR (1999) Coupled ocean–atmosphere dynamics in the Indian Ocean during 1997–98. Nature 401:356–360

Weller E, Cai W (2013) Realism of the Indian Ocean Dipole in CMIP5 models: the implication for climate projections. J Clim. doi:10.1175/JCLI-D-12-00807.1

Wijffels S, Meyers GA (2004) An intersection of oceanic wave guides: variability in the Indonesian through flow region. J Phys Oceanogr 34:1232–1253

Xie S-P, Philander SGH (1994) A coupled ocean-atmosphere model of relevance to the ITCZ in the eastern Pacific. Tellus 46A:340–350

Xie S-P, Annamalai H, Schott FA, McCreary JP (2002) Structure and mechanisms of south Indian Ocean climate variability. J Clim 15:864–878

Yamagata T, Behera SK, Luo J-J, Masson S, Jury MR, Rao SA (2004) Coupled ocean-atmosphere variability in the tropical Indian Ocean. In: Wang C, Xie S-P, Carton JA (eds) Earth climate: the ocean-atmosphere interaction. Geophysical Monograph 147, American Geophysical Union, pp 189–212

Yu W, Xiang B, Liu L, Liu N (2005) Understanding the origins of interannual thermocline variations in the tropical Indian Ocean. Geophys Res Lett 32:L24706. doi:10.1029/2005GL024327

Zheng X-T, Xie S-P, Vecchi GA, Liu Q, Hafner J (2010) Indian Ocean dipole response to global warming: analysis of ocean–atmospheric feedbacks in a coupled model. J Clim 23:1240–1253

Zheng X-T, Xie S-P, Du Y, Liu L, Huang G, Liu Q-Y (2013) Indian Ocean Dipole response to global warming in the CMIP5 multimodel ensemble. J Clim. doi:10.1175/JCLI-D-12-00638.1

Zhong A, Hendon HH, Alves O (2005) Indian Ocean variability and its association with ENSO in a global coupled model. J Clim 18:3634–3649